Materials Science & Engineering A 923 (2025) 147735

Contents lists available at ScienceDirect

Materials Science & Engineering A

journal homepage: www.elsevier.com/locate/msea

High strain rate deformation behavior of QP1180 advanced high-strength steel for automobiles

Shuangjie Chu [a,b], Wenting Zhu [b,*], Bo Mao [b], Guangkui Hu [a]

[a] *Baoshan Iron & Steel Cooperation Limited, Shanghai, 201900, China*
[b] *School of Materials Science and Engineering, Shanghai Jiao Tong University, Shanghai, 200240, China*

ARTICLE INFO

Keywords:
Quenching and partitioning (QP) steel
High strain rate
TRIP effect
Twin martensite
ε-carbides

ABSTRACT

To advance the use of quenching and partitioning (QP) steel in the automotive sector necessitates a comprehensive understanding of its behavior under both static and dynamic loading conditions. Thus, the present article aims at elucidating the effect of strain rate on microstructural alterations and mechanical response in a QP steel with an ultimate tensile strength of 1180 MPa. When the strain rate was elevated from 10^{-3} s^{-1} to 10^{2} s^{-1}, the ultimate tensile strength increased from 1191 MPa to 1318 MPa. Despite substantial transformation of retained austenite into martensite, which activated the transformation-induced plasticity (TRIP) effect, the total elongation initially decreased to 22.2 % before increasing to 29.3 % at a strain rate of 10^{2} s^{-1}. To examine the mechanisms behind this unusual trend in total elongation, the evolution of martensite transformation, twin martensite, carbide precipitation, and dislocation density with strain rate was analyzed via electron microscopy and X-ray diffraction. The results showed that interactions between dislocations and twins reduced the lengths of twin boundaries and exacerbated plastic deformation by inducing severe lattice distortions. In addition, higher strain rates prompted carbon redistribution, leading to carbon clustering and formation of ε-carbides. The shear deformation mechanisms ultimately led to improved strength and ductility as the strain rates increased.

1. Introduction

In recent years, the rapid increase in vehicle populations has exacerbated environmental crises and energy shortages. Given this context, robust support and development of new energy electric vehicles have become critical measures in energy reform. To increase battery life and driving range, electric vehicles have more stringent requirements for weight reduction in comparison to traditional internal combustion engine vehicles. Enhancing the strength of steel is one of the primary methods for achieving material lightweighting [1]. Third-generation advanced high-strength steels (AHSS) represent a novel material class designed to meet the need for high strength while retaining the necessary plasticity for processing [2–4]. Among them, quenching and partitioning (QP) steel demonstrates superior strength compared to dual-phase (DP) steel [5] and transformation-induced plasticity (TRIP) steel [6], with lower alloying element requirements than twinning-induced plasticity (TWIP) steel [7]. The exceptional balance of ductility and strength, along with its relatively low manufacturing costs, positions QP steel among the leading options for large-scale industrial applications. Commercially available QP steels have been widely utilized as critical mechanical components in automobiles, including reinforcements for bumper and B-pillar, longitudinal structural members, and cross members [8].

Extensive investigations of QP steels have focused on the microstructure evolution and mechanical behavior subjected to static tensile loading, as affected by their chemical composition, initial microstructural features, and heat treatment methods [9,10]. While conducting static tensile tests (strain rates$<10^{-2}$ s^{-1}), the transformation of retained austenite to martensite plays a crucial role in accommodating plastic strain and brings about prominent strain-hardening effect. The behavior of deformation-induced martensitic transformation (DIMT) is affected by various factors related to QP steels, including the enrichment of carbon in retained austenite (up to 1-2 wt%) and the distinct morphologies of retained austenite, which can be either film-like or blocky [11].

For automotive body components, however, high-speed impacts constitute a predominant factor contributing to its failure. Instantaneous high stress from collisions or other impactful events in a car body hinders the material from achieving complete plastic deformation capacity, thereby resulting in fractures or brittle failure. Given that the actual strain rates of materials in traffic accidents can reach 10^{2} s^{-1}-10^{3} s^{-1}, it

---

* Corresponding author.
E-mail address: wenting_zhu628@163.com (W. Zhu).

https://doi.org/10.1016/j.msea.2024.147735
Received 27 October 2024; Received in revised form 20 December 2024; Accepted 24 December 2024

is crucial to explore how DIMT behavior affects the work hardening characteristics of QP steels under these high strain rates. Murr et al. [12] and Hecker et al. [13] both indicated that, for AHSS steels, the influence of strain rate on DIMT behavior can be categorized into two main aspects. In one aspect, an increase in strain rate causes a gradual rise in the number of shear bands, consequently enhancing the initiation of the TRIP effect. In contrast, the effect of adiabatic heating during high-speed tensile testing suppresses the dislocation multiplication, twinning, and TRIP effect.

However, some studies on QP steel have revealed contrary results. Finfrock et al. [14] indicated the dynamic tensile properties of a QP980 steel and discovered that the work hardening behavior transitions at a critical threshold of 0.1 s^{-1}. Below this threshold, an increased strain rate suppresses the TRIP effect, whereas above it, the strain rate promotes the TRIP effect. Zou et al. [15] proved the existence of this threshold in QP980 steel. They noted that DIMT is enhanced when strain rates surpass the adiabatic threshold, which can be linked to a higher density of martensite nucleation sites. As noted by Liu et al. [16], the less active TRIP effect observed in QP steel at strain rates below the threshold can be attributed to a growing mechanical driving force due to higher stresses, coupled with a diminishing chemical driving force resulting from adiabatic heating, which impacts DIMT. Indeed, the carbon enrichment and sub-micron grain size of QP steel result in heightened temperature sensitivity. This distinctive characteristic strongly affects deformation mechanisms such as martensitic transformation, twinning, and dislocation glide and multiplication. As the strength grade of QP steel continues to increase, examining the underlying mechanisms of its dynamic deformation presents significant challenges, which may stem from the combination and interaction of several mechanisms mentioned earlier. Xia et al. [17] developed a QP steel characterized by an ultimate tensile strength (UTS) of 1180 MPa and examined the evolution of retained austenite with different morphologies across a broad range of strain rates. Due to significant oscillations in the stress-strain curve at high strain rates, the work hardening behavior was not discussed. To sum up, there have been no systematically reported experimental results or discussions on the deformation mechanisms of QP1180 steel to date.

In the light of this scientific significance and practical implication, a detailed analysis was conducted on the transformation behavior of QP1180 steel across strain rates varying from 10^{-3} s^{-1}-10^{2} s^{-1}. The present work aims to reveal the microstructural evolution and mechanical response of QP steels subjected to tensile loading across a broad spectrum of strain rates, emphasizing the deformation mechanisms that occur at elevated strain rates.

2. Experimental

2.1. Materials

The nominal chemical composition of the QP steel was specified as follows (in wt.%): 0.185C, 1.7Si, 2.7Mn, with the balance being Fe. To offset the reduction in strength resulting from the design characterized by low carbon and low alloy content, the processing routes and parameters of the traditional quenching and partitioning processes were optimized. Consequently, a high-performance, low-cost QP steel with a UTS of 1180 MPa was successfully developed. The quenching temperature and partitioning temperature of this steel are both above 1073 K and 673 K, respectively. In the present study, experimental investigations were conducted on a commercial low-carbon, low-alloy QP1180 steel manufactured by Baosteel (China).

2.2. Tensile testing

Specimens shaped like flat dog-bones were manufactured, with their axes aligned in the direction of rolling. Static tensile tests were carried out using a Zwick Z20 testing machine at two specific strain rates: 0.001 s^{-1} and 0.1 s^{-1}. The experiments were carried out at room temperature, and a mechanical extensometer was employed to measure the strain accurately. Dynamic tensile tests were performed at elevated strain rates between 1 and 100 s^{-1} at room temperature using a Zwick HTM5020 testing machine. A high-speed camera was utilized to capture the two-dimensional deformation of the specimens throughout the testing process. Specimens with a dimension of 10 mm in gauge length and 4 mm in width were used in static tensile tests, while dynamic tensile specimens had a gauge length of 10 mm and a width of 5 mm.

2.3. Microscopy

Scanning electron microscope (SEM) observations and electron backscatter diffraction (EBSD) characterizations were performed by TESCAN MIRA3 electron microscope at 5 kV and 20 kV, respectively. Before SEM observation, the initial specimen was sequentially ground, mechanically polished, and then chemically etched in 4 % (in vol%) nital solution (4 % nitric acid in 96 % alcohol) for 5 s to remove grinding and polishing-induced stress effect. EBSD is employed to analyze phase fractions, grain morphologies, and grain sizes both prior to and following deformation. In preparation for EBSD analysis, the initial specimen underwent mechanical polishing followed by electro-polishing in a mixed solution of nitric acid and alcohol with a volume ratio of 1:7. However, conventional EBSD measurement lacks the spatial resolution required to analyze grains that are severely deformed and sub-micrometer in size. Transmission Kikuchi Diffraction (TKD), also known as transmission EBSD (t-EBSD), was used for studying severely deformed grains. Compared to conventional EBSD, t-EBSD is a newly-developed method in SEM that provides enhanced spatial resolution, making it suitable for characterizing grains under large deformation. Electron-transparent slices for t-EBSD were prepared from the fracture cross-sectional area using a focused ion beam (FIB) milling (TESCAN GAIA3). The EBSD data obtained was analyzed using orientation imaging microscopy (OIM) software.

Further microstructural observations were conducted using high-resolution transmission electron microscopy (HRTEM) on a Talos F200X G2, with an accelerating voltage set to 200 kV. The initial specimen was mechanically thinned down to 60 μm using SiC paper and then punched into 3 mm discs. The disk specimens were electrochemically polished using a Struers TenuPol twin-jet polisher in a mixed solution consisting of 90 % alcohol and 10 % perchloric acid (by volume) at 248 K. For the fractured specimens, the deformation behavior in the vicinity of the fracture was analyzed using HRTEM on the same t-EBSD specimens.

2.4. X-ray diffraction

The preparation of X-ray diffraction (XRD) specimens adhered to the same protocol used for traditional EBSD observations. XRD profiles of the retained austenite were obtained using a Bruker D8 ADVANC instrument, employing Cu $K\alpha$ radiation and covering the range from 40° to 100° in 2.5° increments. The calculation of the volume fraction of retained austenite (V_{RA}) was performed by analyzing the integrated intensities of the BCC peaks at (200), (211), along with the FCC peaks at (200), (220), (311), in accordance with the methodology presented in Eq. (1) [18].

$$V_{\mathrm{RA}} = 1.4 I_{\mathrm{FCC}} / (I_{\mathrm{BCC}} + 1.4 I_{\mathrm{FCC}}) \tag{1}$$

where I_{BCC} and I_{FCC} are the mean integrated intensities of the BCC and FCC diffraction lines, respectively.

3. Results

3.1. Initial microstructure characteristics

Fig. 1(a) shows the SEM image of the initial microstructure of the QP steel. The microstructures subjected to 4 % nital etching can be discerned by their characteristics through SEM. A multiphase microstructure comprising ferrite, martensite and retained austenite was developed in the prior austenite grains. The ferrite (F) exhibited a relatively smooth morphology with a darker background. The tempering martensite (TM), observed after tempering following the first quenching step in the partitioning process, displayed a coarse structure characterized by internal etching features. There was a notable presence of the retained austenite (RA) in Fig. 1(a). XRD measurement was conducted to determine the V_{RA} in the QP steel, yielding an approximate value of 20.9 % based on Eq. (1) (Fig. 1(b)). Bright field (BF) TEM images of the RA in the initial QP specimen are illustrated in Fig. 1(c) and (d). The morphology of the RA manifested in two distinct forms: one characterized by a blocky shape (RA_b), while the other exhibited an elongated, film-like configuration (RA_f). Additionally, some occurrences of martensite-retained austenite constituents (M/RA) were observed, which resulted from the transformation of unstable RA during the final quenching process. As reported by Dai et al. [19], RA_b exhibits a higher propensity to transform to martensite compared to RA_f during deformation due to its lower carbon content.

3.2. Mechanical properties

The engineering stress-strain curves for specimens subjected to tensile loading across a range of strain rates, specifically from 0.001 s^{-1}–100 s^{-1} is illustrated in Fig. 2(a). As shown in the enlarged view of the red rectangle in Fig. 2(a), the curves manifest pronounced and erratic fluctuations when the strain rates reaches or higher than 0.1 s^{-1} (Fig. 2(b)). These variations can be attributed to two fundamental reasons. One reason is the synergistic interplay between softening and hardening behaviors during plastic deformation [20]. Another reason is that when subjected to external loads, all solid materials inherently possess both inertia and deformability. In instances of brief loading times, the rapid spread and interaction of strain and stress within the solid give rise to stress waves, resulting in significant fluctuations in the

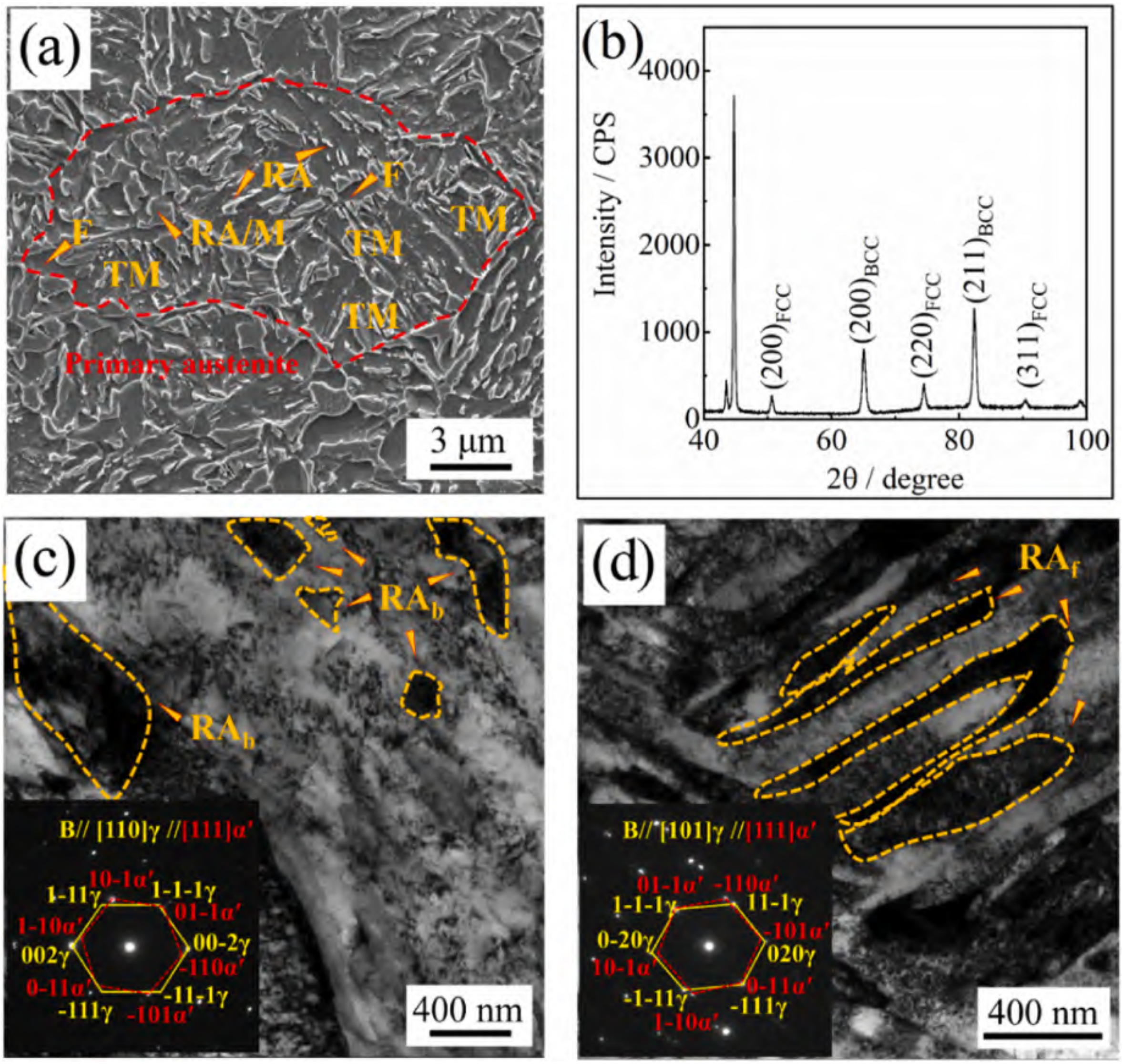

Fig. 1. Examination of the microstructure in the initial QP specimen prior to deformation. (a) SEM image showing the multiple microstructures, including TM, F and RA. Grain boundaries of the primary austenite are highlighted with red-dotted lines. (b) XRD spectra depicting the presence of BCC and FCC. (c, d) BF-TEM images showing the different morphologies of the RA in the initial QP specimen. Displayed in the insets of (c) and (d) are the corresponding selected area electron diffraction (SAED) patterns. (For interpretation of the references to colour in this figure legend, the reader is referred to the Web version of this article.)

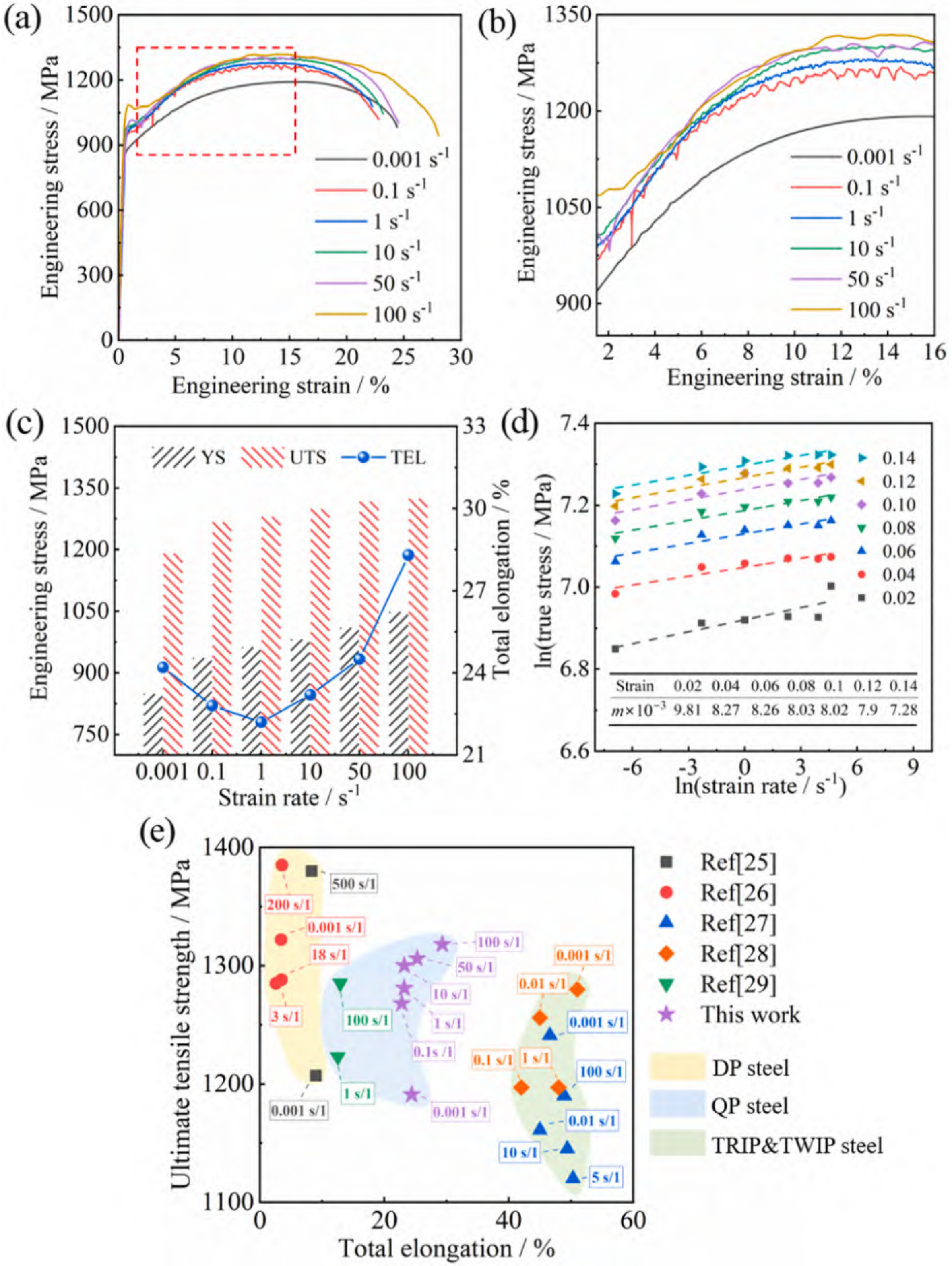

Fig. 2. Mechanical behavior of specimens subjected to tension at various strain rates. (a) Engineering stress-strain curves. (b) Detailed view of the region highlighted in red in (a). (c) Variation in YS, UTS and TEL. (d) True stress versus strain rate in ln-ln coordinates. (e) Ultimate tensile strength versus total elongation for advanced high-strength steels at various strain rates (data marked by stars comes from the present study, all other data were collected form Refs. [25–29]). (For interpretation of the references to colour in this figure legend, the reader is referred to the Web version of this article.)

tensile curves [21]. These tensile results are summarized in Fig. 2(c). Both the yield strength (YS) and UTS exhibited an upward trend with the rise in strain rate from 0.001 to 100 s^{-1}. The YS increased from 850 MPa to 1049 MPa, and the UTS increased from 1049 MPa to 1318 MPa, respectively. However, the total elongation (TEL) was observed to gradually decrease from 24.4 % to 22.2 % upon increasing the strain rate from 0.001 to 1 s^{-1}, while increased dramatically to 29.3 % at 100 s^{-1}.

Fig. 2(d) depicts the bi-logarithmic plots of strain rate against true stress, where the slope of the curves, denoted as m, represents the strain rate sensitivity index. Throughout the plastic deformation process, the m value of flow stress was observed to decline, starting at 0.00981 and reaching 0.00728 as strain advanced. This observation suggested a diminishing strain hardening capability in the QP steel with increasing strain rates. The observed positive sensitivity of tensile strength to strain rates was consistent with the findings reported in dynamic behavior studies of automotive steels by Dong et al. [22], Park et al. [23], and Idrissi et al. [24] However, the variation in TEL of QP steel with strain rate contradicted classical strain rate sensitivity theories for materials with positive strain rate sensitivity. This anomalous strain rate dependence suggests that complex deformation or transition mechanism was involved and will be addressed in the following discussion. Fig. 2(e) summarizes the mechanical properties of advanced high-strength steels at various strain rates, including DP steels, QP steels, TRIP steels and TWIP steels. The QP1180 steel in this study exhibits an exceptional combination of strength and ductility at higher strain rates, approaching the performance of TWIP steels. Moreover, it presents a more cost-effective alternative compared to high-alloy steels.

3.3. *Microstructure evolution*

Fig. 3 shows EBSD micrographs of the initial specimen and specimens fractured under tension at 0.001 s^{-1} and 100 s^{-1}. As shown in Fig. 3(a_1, b_1, c_1), the decrease in V_{RA} was evident subsequent to deformation until failure. The yellow phases in the phase maps represent ε-martensite with an HCP (hexagonal-close packed) structure, considered an intermediate phase in martensitic transformation, whose

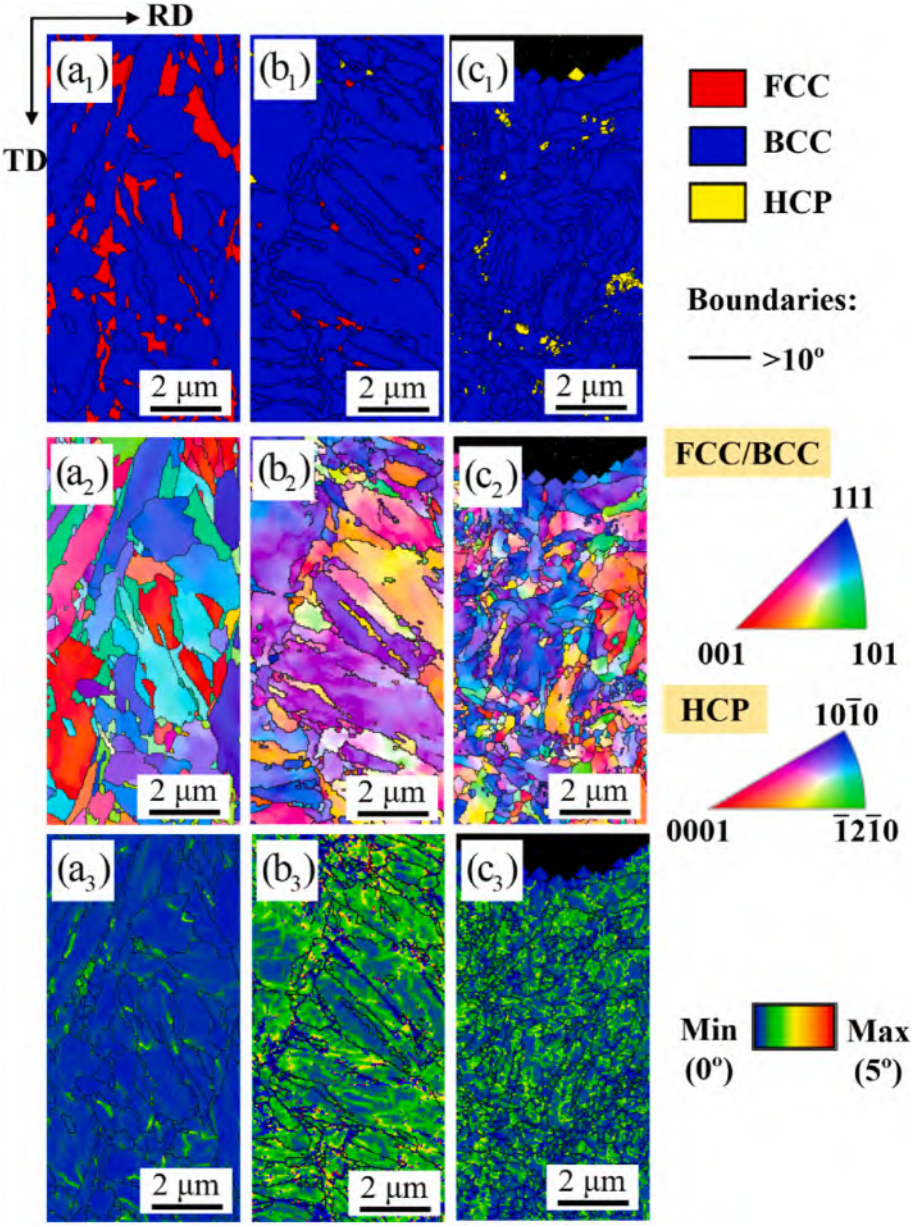

Fig. 3. EBSD comparison of the initial specimen (a_1-a_3), and the specimens deformed to failure at 0.001 s^{-1} (b_1-b_3) and 100 s^{-1} (c_1-c_3). (a_1, b_1, c_1) Phase maps, (a_2, b_2, c_2) IPF maps and (a_3, b_3, c_3) KAM maps.

volume fraction increases with strain rate. Additionally, raising the strain rate not only resulted in a reduction of V_{RA} but also led to a decrease in grain size. The specimen deformed at 100 s^{-1} showing an average size of 0.55 μm, compared to 2.3 μm and 2.8 μm for those deformed at 0.001 s^{-1} and the initial specimen, respectively (Fig. 3(a$_2$, b$_2$, c$_2$)). EBSD orientation maps were utilized to evaluate local misorientations in grains, aiming to provide a quantitative assessment of dislocation densities in specimens tested under varying strain rates during tension. The kernel average misorientation (KAM) map was chosen as the indicator for this analysis and the results were presented in Fig. 3(a$_3$, b$_3$, c$_3$). However, the KAM distributions revealed a decrease in local crystallographic rotation within the BCC phase under elevated strain rates.

Fig. 4 presents the XRD patterns and corresponding quantitative results for undeformed and fractured QP specimens under various strain rates. A substantial amount of RA has transformed into martensite regardless of strain rate, as evidenced by comparing the V_{RA} of the deformed specimen (Fig. 4(b)) with that of the undeformed specimen shown in Fig. 1(b). The V_{RA} exhibits a slight increase from 6.9 % to 8.8 % as the strain rate progresses from 0.001 up to 50 s^{-1}, while drops to 5.9 % at 100 s^{-1}.

4. Discussion

4.1. The underlying mechanisms governing the serrated flow behavior

Serrated flow associated with plastic instability was observed in the tensile curves across various strain rates (Fig. 2(b)). Recent studies suggest that the serrated flow behavior arises from the Portevin-Le Chatelier (PLC) effect, typically influenced by dynamic interactions occurring between solute atoms and mobile dislocations in the process of tensile [30,31]. The PLC effect in medium-Mn steel has been studied quantitatively studied using *ex situ* XRD method and DIC technique [32]. Given the excessively high strain rates, it is not feasible to gather the aforementioned experimental information during dynamic deformation. Hence, this study analyzed the PLC effect by examining the serrated fluctuations in the curves of true stress-strain and strain hardening rate at varying strain rates. Latest research findings [33,34] categorize serrated flow and PLC band propagation in true stress-strain curves into three classifications: 1) Type A serration, characterized by a sharp rise in flow stress, succeeded by a swift return to the baseline stress level; 2) Type B serration, which involves oscillations in stress that rise and fall along the curve; 3) Type C serration, identified by rapid decreases in stress, typically seen beneath the stress-strain curve, followed by recoveries.

Fig. 5(a) illustrates the true stress-strain curves in conjunction with the associated strain hardening rate (SHR) curves of QP steel across various strain rates. Among them, the SHR curves were smoothed to better elucidate serrated flow behavior and deformation mechanisms. As shown in Fig. 5(b), QP steel deformed at 0.001 s^{-1} exhibited a distinct three-stage strain hardening behavior. The deformation process began with a rapid drop in the SHR during its initial stage, which was later accompanied by either an increase or a plateau. After that, a sustained decrease in the SHR was observed. Drawing from a majority of studies on steels with Mn content ranging from 2 % to 5 % [35,36], the strain hardening stage is initiated by the deformation of ferrite, transitions into a stage driven by the TRIP effect, and ends with a stage characterized by a diminished potential for martensitic transformation. Due to sufficient deformation time, the second stage showed a continuous downward trend for the specimen deformed at 0.001 s^{-1}.

As the strain rate reached 0.1 s^{-1}, there were noticeable fluctuations in the SHR curve (Fig. 5(c)). Moreover, the true stress-strain curve revealed clear serrations, primarily dominated by Type A serrations. Nam et al. [37] highlighted a connection between Type A serrated flow and the intermittent TRIP effect, wherein localized fresh martensite formed by DIMT appear in the PLC bands during tensile deformation in medium Mn steel. Similar results were confirmed by Cai et al. [38] In Fig. 5(c), a significant sharp rise in the SHR was evident between points a$_1$ and a$_2$, followed by a subsequent decrease ranging from points a$_2$ to a$_3$. The increased SHR can be attributed to the initiation and growth of Type A serrated flow, in conjunction with DIMT. As stress accumulated, the SHR decreased. This implied that the movement of Type A PLC bands encountered obstacles, resulting in the redistribution of local stress. Once the stress exceeded a critical threshold, the TRIP effect was reactivated, leading to the reappearance of Type A serration (from points a$_3$ to a$_4$). Variations in the stability of RA caused the described process to occur repeatedly as strain increased, resulting in a discontinuous TRIP effect.

To elucidate the relationship between strain rate and the mechanisms of plastic deformation of QP steels, particular attention should be paid on the adiabatic heating generated during tensile tests. Such a localized increase in temperature may result in the thermodynamic instability of RA, thereby affecting its phase transformation and mechanical properties. For instance, the temperature increases by 293–298 K for the 6Mn-1.5Si alloy (TEL: 10–22 %) deformed at 0.001 s^{-1} [39]. Meanwhile, in the Cr-Ni-Mo-Si-Mn alloy (TEL: 23 %) deformed at a

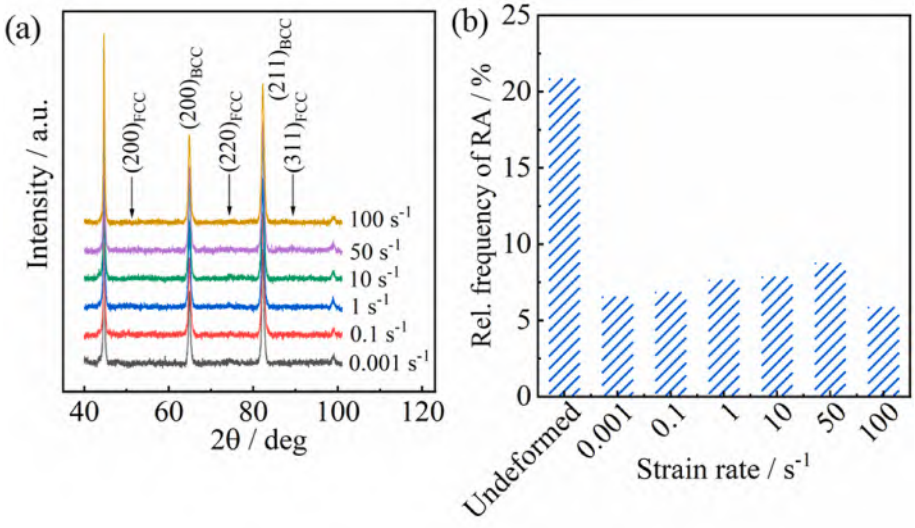

Fig. 4. XRD results of tensile specimens tested under varying strain rates. (a) XRD patterns. (b) Variation in the V_{RA}.

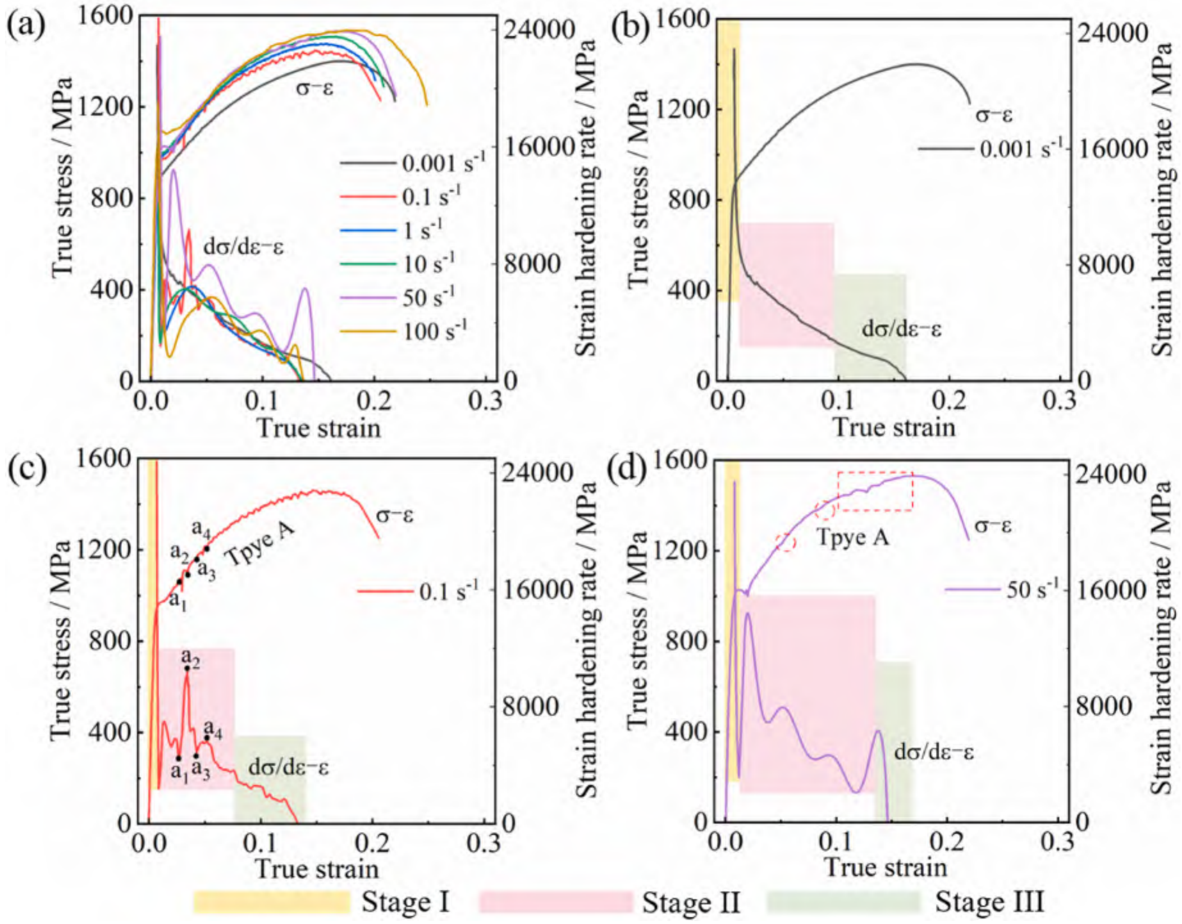

Fig. 5. True stress (σ) and strain hardening rate (dσ/dε) as functions of true strain (ε) for specimens tensioned at all tested strain rates (a), and at specific strain rates of 0.001 s^{-1} (b), 0.1 s^{-1} (c), 50 s^{-1} (d).

higher rate of 0.1 s^{-1}, the temperature elevation exceeds 315 K [40]. In contrast, QP steel have comparatively lower thermal conductivity. The rise in adiabatic temperature became more pronounced as the strain rate increased. Due to the significantly shortened deformation time when strain rates exceed 0.1 s^{-1}, heat dissipation is regarded as negligible. Thus, the increase in temperature becomes crucial during dynamic deformation, and its incremental value ΔT can be calculated using Eq. (2) [41]:

$$\Delta T = \frac{dQ}{m_\rho C_\rho} = \frac{\beta\eta}{m_\rho C_\rho}\sigma d\varepsilon \tag{2}$$

$$\eta = \begin{cases} 0 & \dot{\varepsilon} < 10^{-3} \\ 0.25\log(\dot{\varepsilon}) + 0.75 & 10^{-3} \le \dot{\varepsilon} \le 1 \\ 1 & \dot{\varepsilon} > 1 \end{cases} \tag{3}$$

where dQ refers to the heat energy, m_ρ to the steel density, β to the fraction of mechanical energy converted into heat energy, C_ρ to the specific heat capacity, η to the adiabatic correction factor. Here, m_ρ = 7.85 g•cm^{-3}, $C_\rho = 0.45$ J kg^{-1} K^{-1}, $\beta = 0.95$. The adiabatic correction factor η, which is mainly related to the strain rate, is expressed by Eq. (3) [42]. As calculated, the variation in adiabatic temperature rise for QP1180 steel subjected to various strain rates is summarized in Table 1.

Findings from Murr et al. [12] and Hecker et al. [13] suggest that adiabatic heating could potentially hinder the TRIP effect. However, given the similar proportion of RA undergoing transformation to martensite across various strain rates (Fig. 4), there appeared to be a competitive relationship between the influences of stress and temperature regarding the martensitic transformation kinetics. This competition resulted in the TRIP effect contributing similarly to the mechanical properties of QP steel under different testing conditions. During Stages II and III, the SHR curves demonstrated less pronounced fluctuations when strain rates were within the range of 0.1 and 10 s^{-1} (Fig. 5(a)). However, at strain rates of 50 s^{-1} and above, noticeable fluctuations in the SHR reappeared (Fig. 5(d)). As the deformation rate increased, the nucleation and propagation of Type A PLC bands were inhibited. Therefore, it is reasonable to infer that the TRIP effect in QP steel is not the only deformation mechanism when subjected to higher strain rates. Other deformation mechanisms are likely to be involved during the tensile test.

Table 1
Variation in adiabatic temperature rise with respect to strain rate.

Strain rate/s^{-1}	0.1	1	10	50	100
Adiabatic temperature rise/K	35.6	52.7	74.5	79.3	91.1

4.2. *Interaction between twins and dislocations*

Fig. 6 displays the typical microstructure of the initial specimen as observed by TEM. Martensite is categorized into two different types based on their carbon concentrations: carbon-depleted lath martensite (Fig. 6(a)) and carbon-enriched twinned martensite (Fig. 6(b)). Tempering during the partitioning process results in dislocation cells forming within the laths present in lath martensite through recovery [43]. Additionally, some dislocations that had decomposed were noted on the exterior of the twin martensite. Fig. 6(c) and (d) depict the dark field (DF) TEM image and the corresponding SAED pattern of the twin martensite from Fig. 6(b), respectively. The twin boundaries had an

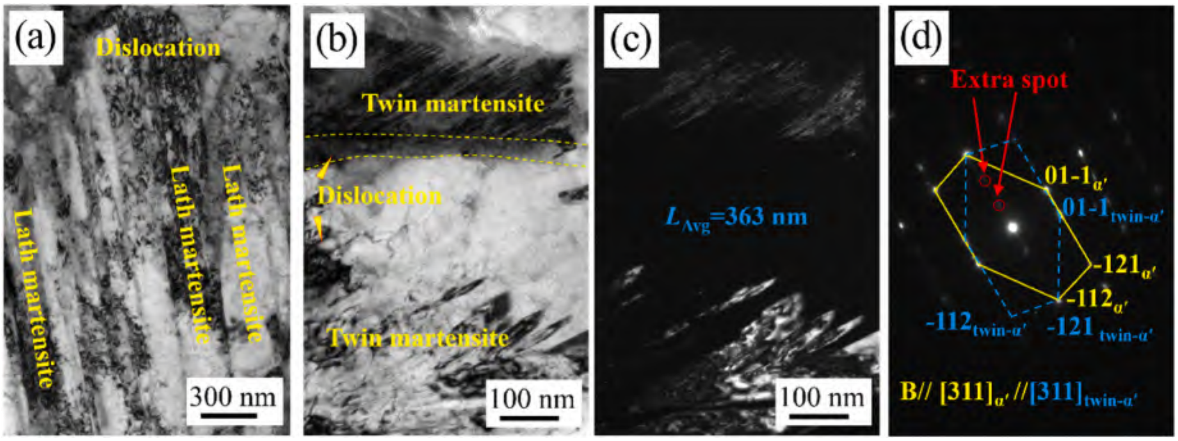

Fig. 6. TEM micrographs of the typical microstructure of the initial specimen. (a) BF-TEM image of the lath martensite. (b, c) BF-TEM image and corresponding DF-TEM image of the twin martensite, respectively. (d) SAED pattern of the twin martensite. Twin martensite: twin-α′

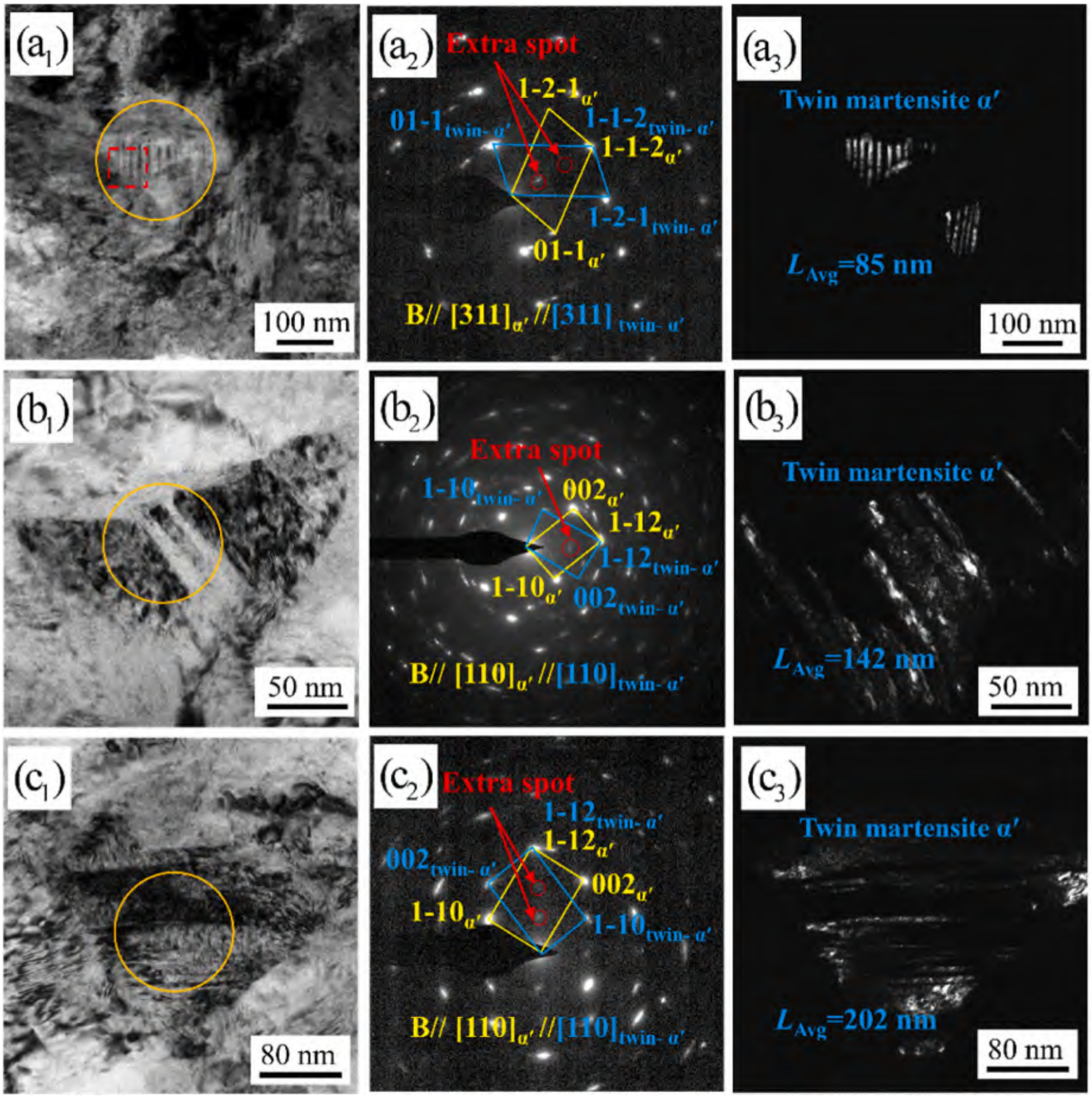

Fig. 7. Characteristics of twin martensite near the fracture in the specimens tensioned at 0.1 s^{-1} (a_1-a_3), 50 s^{-1} (b_1-b_3), and 100 s^{-1} (c_1-c_3). (a_1, b_1, c_1) BF-TEM images, (a_2, b_2, c_2) SAED patterns and (a_3, b_3, c_3) DF-TEM images.

average length (L_{Avg}) of about 363 nm. In the upper portion of the DF-TEM image, nanoscale ultrafine twin lamellae in the twin martensite were clearly visible. Conversely, the width of the twin laths at the bottom of the DF-TEM image exhibited a marked increase.

Fig. 7 presents the BF-TEM images (a_1, b_1, c_1), SAED patterns (a_2, b_2, c_2), and DF-TEM images (a_3, b_3, c_3) of an area containing twin martensite near the fracture in the specimens tensioned at 0.1 s^{-1} (a_1-a_3), 50 s^{-1} (b_1-b_3), and 100 s^{-1} (c_1-c_3). The SAED pattern was obtained using a focused approach on the regions outlined by the orange circle in Fig. 7(a_1) to achieve clear diffraction spots (Fig. 7(a_2)). From the [311] zone axis, two overlapping diffraction patterns of martensite exhibiting a twinning relationship can be discerned. Interestingly, an additional periodic diffracted spot was observed that did not correspond to either martensite or twins (Fig. 7(a_2)). The DF-TEM image (Fig. 7(a_3)) corresponding to the extra diffracted spot highlighted in Fig. 7(a_2) shows a pronounced band contrast along the twin boundaries. The L_{Avg} of the nanoscale twin boundaries was measured to be 85 nm. Compared to the initial specimen (Fig. 6(c)), the average length of the twin boundaries in the specimen tested at 0.1 s^{-1} has significantly decreased. As illustrated in Fig. 7(b_1-b_3) and Fig. 7(c_1-c_3), for the specimens tensile tested at 50 s^{-1} and 100 s^{-1}, the average lengths of the twin boundaries increased to 142 nm and 202 nm, respectively.

The variation in twin length with strain rate is closely related to dislocation density. The modified Williamson-Hall (MWH) method can be used to determine the average dislocation density in QP steel using XRD data [44].

$$\Delta K - \beta W_{\text{hkl}} = 0.9 \Big/ \text{D} + \left(\pi \text{M}^2 \text{b}^2/2\right)^{1/2} \rho^{1/2} \left(KC^{1/2}\right) \tag{4}$$

where ΔK refers to the full width at half maximum, β to a variate, W_{hkl} to a factor used to quantify the peak broadening induced by stacking faults in various *hkl* reflections. D, b and ρ represent the average particle size, the Burgers vector and dislocation density, respectively. M is a dimensionless constant. This determined by the outer cut-off radius of dislocations. Additionally, K represents the norm of the scattering vector as defined by Eq. (5), while C denotes the contrast factor of dislocations as outlined in Eq. (6).

$$K = 2\sin\theta/\lambda \tag{5}$$

$$C = 0.285\left(1 - q\frac{h^2k^2 + k^2l^2 + h^2l^2}{h^2 + k^2 + l^2}\right) \tag{6}$$

Among them, λ and θ are the wavelength of the X-ray and the diffraction angle, respectively. q is the fraction of edge and screw dislocation, h, k, l are the Miller's indices of each peak of BCC [45].

Based on Eq. (5), the 2θ values on the horizontal axis (Fig. 1(b)) are converted to K, and the diffraction profile of the initial specimen obtained by fitting with a Lorentz function is shown in Fig. 8(a). From this, ΔK can be derived from the curve fitted using the Lorentz function. Based on the previous studies [46–48], the values of W_{hkl}, C and β can be obtained, and therefore, a scatter plot of $\Delta K - \beta W_{\text{hkl}}$ and $KC^{1/2}$ is subsequently generated and subjected to linear regression analysis. Thus, the slope presented in Fig. 8(b) is representative of $\left(\pi A^2 b^2/2\right)^{1/2} \rho^{1/2}$. Given that π, b, and M are constants, the value of ρ can be determined. As computed, the ρ value of the initial QP specimen is approximately 4.5 × 10^{14} m^{-2}. While, the ρ values for QP specimens subjected to varying strain rates are only estimated and indicated in Table 2.

As listed in Table 2, the dislocation density initially grows as the strain rate increases, but once the strain rate exceeds 50 s^{-1}, it begins to decrease. This variation in dislocation density corresponds to the results illustrated in the KAM map shown in Fig. 3. The increased strain rate primarily enhanced dislocation slips in the deformation substructure, thereby influencing the microstructural evolution of the QP specimen. HRTEM analyses disclose detailed microstructural characteristics of the interactions between twins and dislocations within the rectangular region marked by the red dots in Fig. 7(a_1), as depicted in Fig. 9. The region enclosed by the yellow-dotted rectangle in Fig. 9(a) is further magnified in Fig. 9(b). From this magnification, it was evident that the atomic arrangement along the twin boundaries appeared blurred and distorted, providing evidence that some interaction occurred at these boundaries. To illustrate this phenomenon, inverse fast Fourier transform (IFFT) lattice fringe images (Fig. 9(d) and (e)) were reconstructed from the $(01{-}1)_{\text{twin-}\alpha'}$ and $(0{-}11)_{\text{twin-}\alpha'}$ spots marked with red circles, as well as the $(01{-}1)_{\alpha'}$ and $(0{-}11)_{\alpha'}$ spots marked with green circles in Fig. 9(c), respectively. A series of dislocations, denoted by white "T"s, were observed near the twin boundaries under a strain rate of 0.1 s^{-1}. They were generated by the stress due to tensile deformation. These dislocations are likely to undergo rotation, dissociation, and reconstruction upon impinging on the twin boundaries, leading to a reduction in the length of nanoscale twin boundaries, as shown in Fig. 9(f). Dislocations moving toward the twin boundaries can transmit strain and cause significant stress/strain concentration around the twin martensite [49]. This is supported by the severe lattice distortion observed in region R1 of Fig. 9(b). Such stress concentration is prone to fasten local failure. When a certain strain rate is reached, a reduction in dislocation density occurs, as indicated in Table 2. This variation is attributed to the local adiabatic temperature rise, which suppresses the interaction between

Table 2
Variation in dislocation density (ρ: 10^{14}) of QP specimens subjected to different strain rates.

Strain rate/s^{-1}	0	0.001	0.1	1	10	50	100
Dislocation density/ m^{-2}	4.5	15.6	15.8	15.8	16.1	14.4	14.2

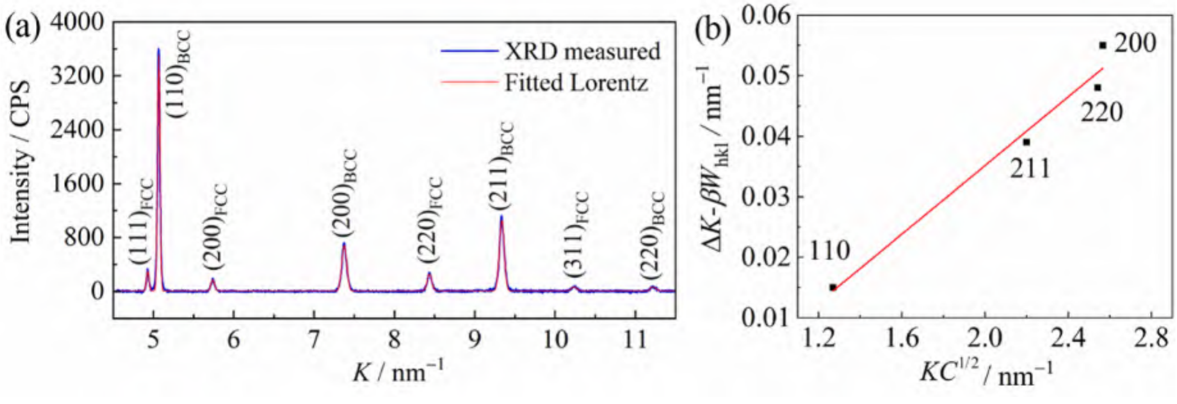

Fig. 8. The MWH analysis for the initial QP specimen. (a) XRD data with corresponding Lorentzian fit. (b) $\Delta K - \beta W_{\text{hkl}}$ versus $KC^{1/2}$ scatter plot.

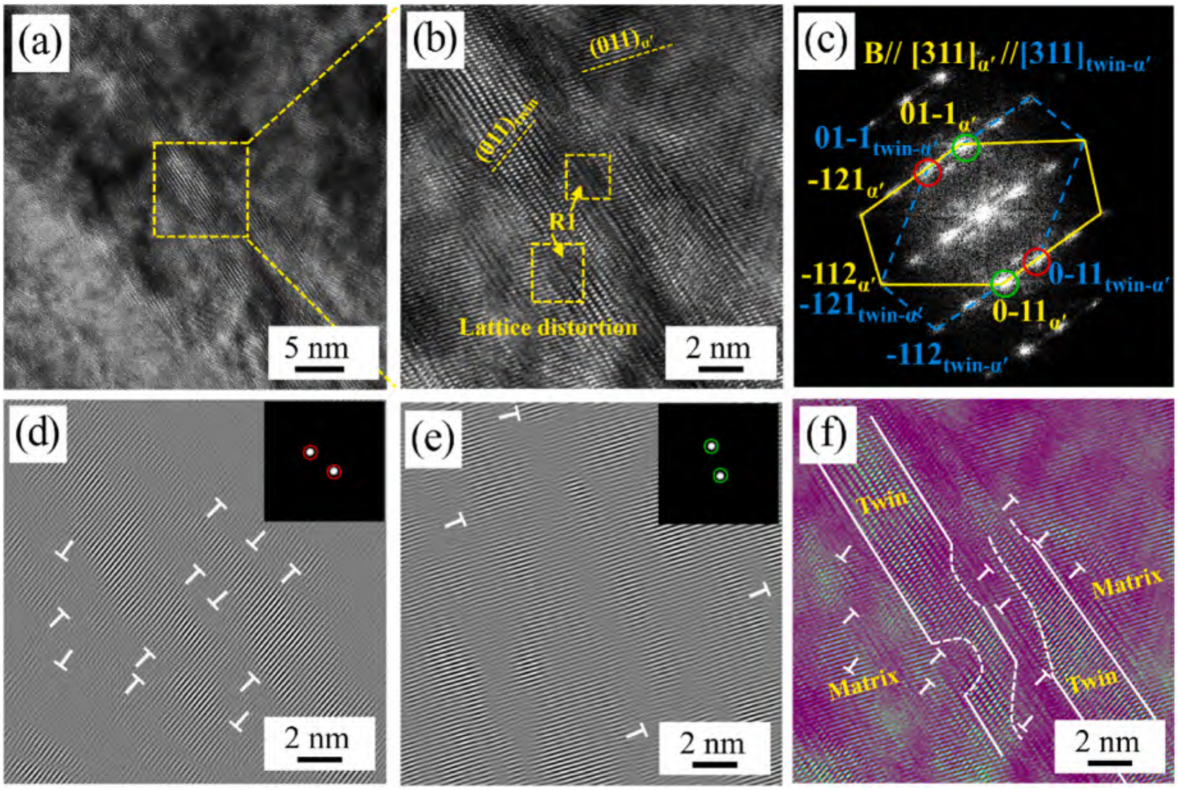

Fig. 9. Detailed TEM observations of the specimen tensioned at 0.1 s^{-1}. (a) HRTEM image showing twin martensite marked by the red-dotted rectangle in Fig. 7(a). (b) Enlarged HRTEM image of the region in the yellow-dotted rectangle from (a). (c) Corresponding FFT pattern. (d, e) IFFT lattice fringe images reconstructed using the twin-α′ and α′ reflections enclosed by red circles and green circles in (c), respectively. (f) RGB composite image combining (b) (green channel) and (d) (red and blue channel). Dislocations are indicated by white "T"s. (For interpretation of the references to colour in this figure legend, the reader is referred to the Web version of this article.)

twins and dislocations (Fig. 7(b_3, c_3)).

4.3. *The mechanism of ε-carbide formation*

Based on research from Zhang et al. [50] and Tkachev et al. [51], it is known that ε-carbide rarely exists in QP steel processed at higher tempering temperatures (above 673 K), which corresponds to the observations in this initial QP1180 steel. High temperatures promote the diffusivity of carbon, leading to the preferential precipitation of more stable carbides, such as η-carbide or θ-carbide, rather than ε-carbide. Through TEM characterization of specimen that had undergone deformation at higher strain rates, ε-carbides were observed unexpectedly and assumed to significantly influence the plastic deformation of the steels. Fig. 10(a) shows a BF-TEM image illustrating the morphology of precipitates in the specimen that fractured at 100 s^{-1}. Some film-like carbides with dimensions between 150 and 200 nm were observed in the martensite. Nano-beam diffraction was performed on the region outlined in red circle in Fig. 10(a), and the resulting nano-beam diffraction pattern is presented in Fig. 10(b). The alignment of the martensite phases with the ε-carbides follows the Jack-orientation relationship [52]: [11−20]ε-carbides//[001]α′, (0002)ε-carbides//(101)α′, (1−100)ε-carbides//(−101)α′. Based on the Jack-orientation relationship, there is a favorable alignment between the [0002]ε and [1−100]ε orientations with the [101]α′ and [−101]α′ orientations, respectively. Furthermore, this alignment implies that ε-carbides are potentially extended along the [010]α′ direction, exhibiting facet interfaces on both the (101)α′ and (−101)α′ planes.

Generally speaking, temperature and loading act as the primary factors driving the migration and redistribution of carbon atoms in martensite, ultimately leading to the formation of ε-carbides [53]. Presented in Fig. 10(c) and (d) are the HRTEM image depicting the film-like carbides from region R2 of Fig. 10(a) and its corresponding fast Fourier transform (FFT) pattern, respectively. The ε-carbides in Fig. 10(c) do not exhibit semi-coherent interfaces, suggesting an absence of significant lattice rotation and lattice mismatch between them. Observation of the green-dotted lines in Fig. 10(c) revealed that the interface on the (101)α′ plane was incoherent, while the interface on the (−101)α′ plane was coherent. Consequently, the interface on the (101)α′ plane was considered to be less energetically favorable compared to the interface on the (−101)α′ plane. Fig. 10(e) depicts an HRTEM image of region R3 from Fig. 10(a). A notable finding was the presence of cellular contrasts enclosed by {011}α′ boundaries. The dimensions of these cells, indicated by the red-solid boxes, were approximately 1.31 nm in length and 0.88 nm in width.

The FFT pattern represented in Fig. 10(f) corresponds to the region outlined with yellow-dashed lines in Fig. 10(e). It was evident that no splitting of (101)α′ spots was observed, whereas the spots of (−101)α′ exhibited distinct splitting, as denoted by the two red arrows. Upon close examination of the FFT pattern, it was observed that the splitting direction of the (00–2)α′ spot deviated from the [001]α′ direction, suggesting that the carbon clusters experienced a rotation with an estimated deflection angle of approximately 3.3°. It has been established in prior research that shear deformation is induced along the {011}α′ planes due to such tetragonal distortion in the BCC matrix [54]. This deformation subsequently promotes the precipitation of ε-carbides. In addition, the tetragonal distortions observed in the carbon clusters with a body-centered tetragonal (BCT) structured led to deviations of {110} planes from their designated positions, which indicated that the role of lattice rotation was pivotal in the atomic displacements. These cellular structures are considered to be an intermediary phase in the process where carbon clusters contribute to the formation of ε-carbides [55].

Fig. 11 depicts a schematic representation of the transition process

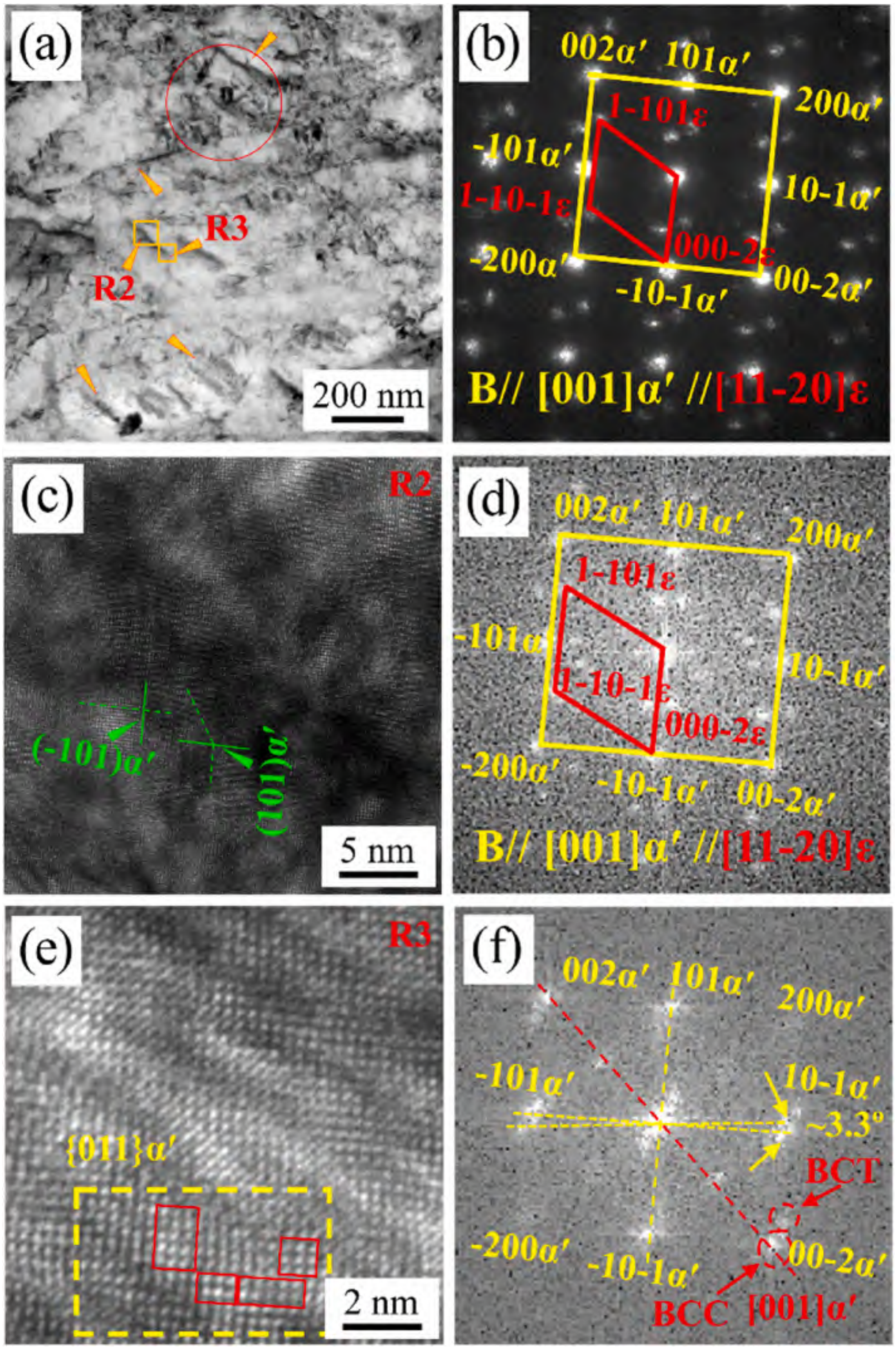

Fig. 10. TEM micrographs of ε-carbides in the specimen deformed at 100 s^{-1}. (a) BF-TEM image. (b) Nano-beam diffraction pattern. (c, d) HRTEM image and the corresponding FFT pattern of region R2. (e, f) HRTEM image of region R3 and the corresponding FFT pattern from the yellow-dotted rectangle in (e). (For interpretation of the references to colour in this figure legend, the reader is referred to the Web version of this article.)

from carbon clusters to ε-carbides. The lattice spacings of (11–20)ε and (002)α′ were measured to be 2.73 Å and 2.87 Å, respectively. When there are minimal differences in lattice spacings, the atomic interactions are stronger, which facilitates shear deformation [54,56]. This lends support to the mechanisms by which carbon clusters undergo shear deformation, leading to the formation of ε-carbides on the {110}α′ plane. Such lattice rotation within carbon clusters causes cellular structures to form that relieve strain, similar to the cellular dislocations commonly seen in ferritic steels subjected to deformation [57]. This process contributes positively to ductility. Moreover, the formation of ε-carbides consumes carbon atoms that were originally in solid solution in the steel, thereby suppressing the PLC effect.

The multiple deformation mechanisms impart QP1180 steel with a higher strength-ductility balance of 38.6 GPa·% (UTS × TEL) at 100 s^{-1} compared to most other QP steels [58,59]. Given the complex deformation behavior of QP1180 steel involving multiple phases (retained austenite, ferrite and martensite), a schematic diagram illustrating its deformation mechanisms at increasing strain rates has been prepared to aid comprehension, as shown in Fig. 12. In Figs. 1 and 6, the undeformed QP steel includes blocky and film-like forms of retained austenite, along with lath-like martensite, twin martensite, and ferrite. There is a notable disparity in dislocation density between the martensite and ferrite (Fig. 12(a)). Upon increasing the strain rate to 0.1 s^{-1} (Fig. 12(b)), the dislocation density increases from 4.5 × 10^{14} to 15.8 × 10^{14} m^{-2}

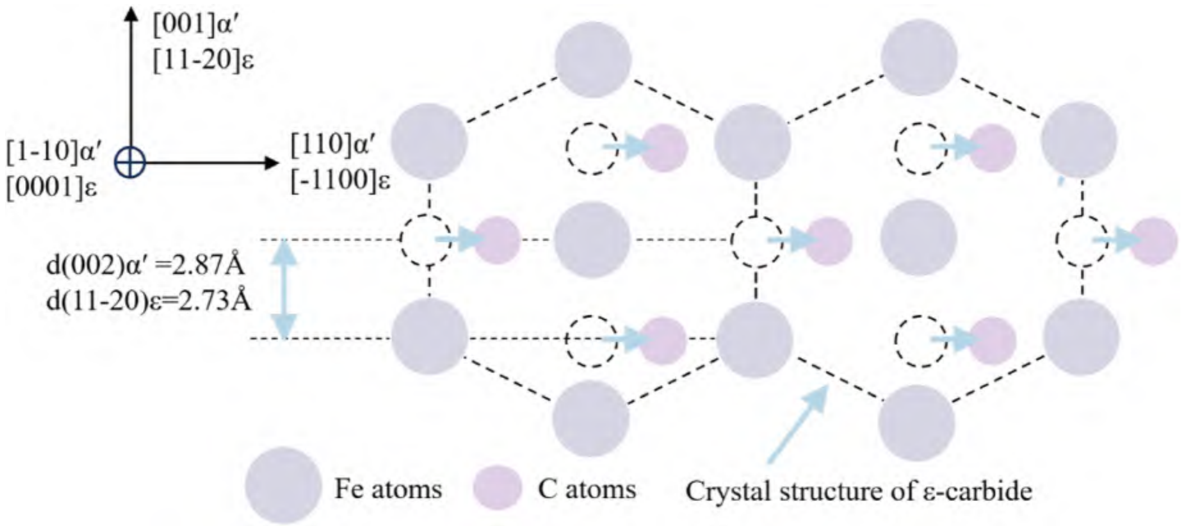

Fig. 11. Schematic representation of the transition process from carbon clusters to ε-carbides.

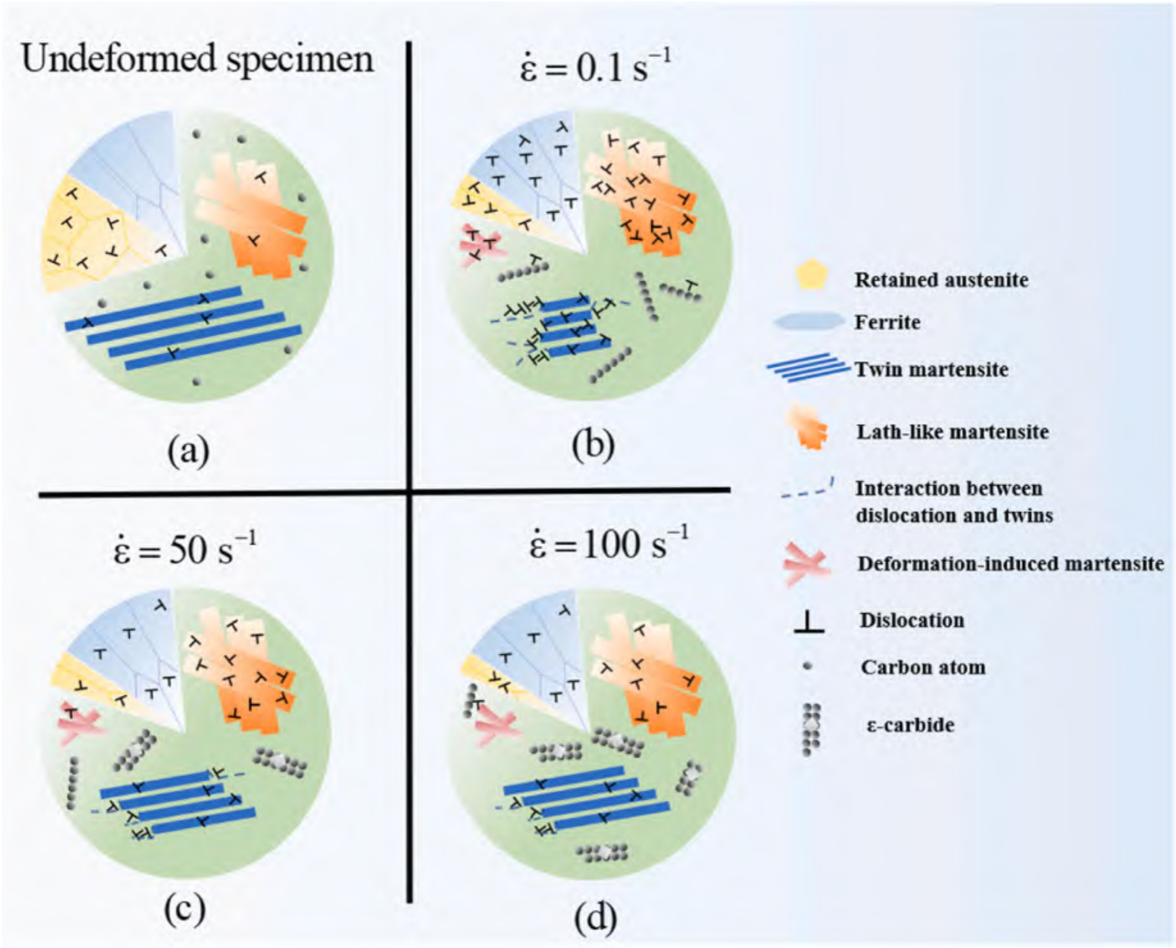

Fig. 12. A diagram depicting the deformation mechanisms in QP1180 steel with increasing strain rates.

(Table 2). Dislocation strengthening, coupled with the TRIP effect, collectively contributes to the enhancement of strength. A significant accumulation of dislocations interacts with the twins, altering their misorientation and reducing the twin length from 363 nm to 85 nm (Fig. 6(c) and 7(a_3)). However, this interplay causes severe lattice distortion and reduces the total elongation (Fig. 2). With a further increase in strain rate, a strain rate of 50 s^{-1} can induce adiabatic temperature rises of up to 79.3 K and decrease the dislocation density to $14.4 \times 10^{14}\ m^{-2}$ (Table 2). These interactions between dislocations and twins are thereby suppressed, leading to longer twin lengths than those observed at 0.1 s^{-1}. With increasing adiabatic temperature and applied loading, carbon atoms in a supersaturated solid solution group together to create clusters, which subsequently facilitate the precipitation of ε-carbides. This precipitation process may be enhanced by mechanisms involving both shear deformation and lattice rotation. Due to the relatively consistent retained austenite content observed after tension across various strain rates (Fig. 4), it can be concluded that the TRIP effect has a negligible influence on variations in both strength and ductility. Thus, the increase in strength and ductility of QP steel tensile fractured at 50 s^{-1} is attributed to precipitation strengthening and shear deformation mechanisms. Finally, QP1180 steel strained at 100 s^{-1} achieves a high UTS of 1318 MPa and a high TEL of 29.3 % through multiple deformation mechanisms.

5. Conclusions

A comprehensive investigation was conducted on the dynamic deformation behavior of low-carbon and low-alloy QP1180 commercial steel developed by Baosteel, using a high-speed tensile testing machine to simulate its response during actual automotive collision conditions. Tensile tests at a static state were also conducted for comparison. Based on the experimental results, the following conclusions can be drawn.

1. QP1180 steel shows positive strain rate sensitivity across a wide range of strain rates from 10^{-3}–10^{2} s^{-1}. Both the yield strength and ultimate tensile strength increase linearly with strain rate. The total elongation exhibits an initial decline followed by a subsequent increase.
2. The evolution trends of martensitic transformation are similar for deformation at different strain rates, indicating that the TRIP effect is not responsible for the variation in strength and ductility.
3. TEM observations confirm that the reorientation of twin boundaries occurs when dislocations traverse or collide with them, leading to a decrease in the length of twin boundaries. These shorter twin boundaries restrict dislocation slip and rearrangement, thereby reducing plastic deformation capacity.
4. ε-carbide formation was identified in the QP steel as deformed at high strain rates. It was assumed that the occurrence of ε-carbide was resulted from the redistribution of carbon due to the prominent adiabatic heating during high strain rate plastic deformation. Moreover, transformation of carbon clusters to ε-carbide contributes to the enhanced plasticity and weakened PLC effects.

CRediT authorship contribution statement

Shuangjie Chu: Writing – original draft, Resources, Project administration, Investigation, Funding acquisition, Conceptualization. **Wenting Zhu:** Writing – review & editing, Writing – original draft, Supervision, Formal analysis, Data curation. **Bo Mao:** Writing – review & editing, Methodology, Funding acquisition. **Guangkui Hu:** Resources.

Declaration of competing interest

The authors declare that they have no known competing financial interests or personal relationships that could have appeared to influence the work reported in this paper.

Acknowledgments

This work was financially supported by the National Natural Science Foundation of China (General Program No. 52101046) and Baoshan iron and steel Co. Ltd. (No. 24H010101558)

Data availability

Data will be made available on request.

References

[1] B.H. Sun, K.D.S. Alisson, Y.X. Wu, Y. Ma, H. Chen, C. Scott, D. Ponge, D. Raabe, Int. Mater. Rev. 68 (2023) 786–824.
[2] P. Jovičević-Klug, M. Jovičević-Klug, L. Thormählen, J. McCord, M. Rohwerder, M. Godec, B. Podgornik, Mater. Sci. Eng. A 873 (2023) 145033.
[3] M. Moshtaghi, E. Maawad, A. Bendo, A. Krause, J. Todt, J. Keckes, M. Safyari, Mater. Des. 234 (2023) 112323.
[4] Y.J. Li, G. Yuan, L.L. Li, J. Kang, F.K. Yan, P.J. Du, D. Raabe, G.D. Wang, Science 379 (2023) 168–173.
[5] D. Ren, C.C. Wang, X.L. Wei, Q.Q. Lai, W. Xu, Acta Mater. 252 (2023) 118954.
[6] Y.D. Shi, A. Zhang, S.X. Liang, X.L. Zhang, S. Ren, H.J. Liu, D. Xu, X.R. Yang, Z. G. Xing, L.N. Wang, Mater. Sci. Eng. A 893 (2024) 146131.
[7] S.C. Shen, P. Xie, C.L. Wu, J. Luo, H.F. Ye, J.H. Chen, Int. J. Plast. 175 (2024) 103922.
[8] L. Wang, J.G. Speer, Metallogr. Microstruct. Anal. 2 (2013) 268–281.
[9] A. Kozłowska, G. Kokot, K. Matus, A. Grajcar, Theor. Appl. Fract. Mech. 133 (2024) 104520.
[10] D.K. Kim, H.J. Kim, S. Gong, S.E. Shin, S.J. Lee, Tribol. Int. 194 (2024) 109445.
[11] H.Q. Zheng, J.Z. Zhang, X.W. Zuo, Y.H. Rong, J.F. Wan, N.L. Chen, Int. J. Plast. 175 (2024) 103928.
[12] L.E. Murr, K.P. Staudhammer, S.S. Hecker, Metall. Trans. A 13 (1982) 627–635.
[13] S.S. Hecker, M.G. Stout, K.P. Staudhammer, J.L. Smith, Metall. Trans. A 13 (1982) 619–626.
[14] C.B. Finfrock, M.M. Thrun, D. Bhattacharya, T.J. Ballard, A.J. Clarke, K.D. Clarke, Metall. Mater. Trans. A 52 (2021) 928–942.
[15] D.Q. Zou, S.H. Li, J. He, Mater. Sci. Eng. A 680 (2017) 54–63.
[16] C. Liu, L. Wang, Y. Liu, Mater. Sci. Forum 749 (2013) 401–406.
[17] P.K. Xia, F. Vercruysse, R. Petrov, I. Sabirov, M. Castillo-Rodríguez, P. Verleysen, Mater. Sci. Eng. A 745 (2019) 53–62.
[18] A. Panda, L. Davis, P. Ramkumar, M. Amirthalingam, Int. J. Hydrogen Energy 58 (2024) 1359–1371.
[19] Z.B. Dai, H. Chen, R. Ding, Q. Lu, C. Zhang, Z.G. Yang, S.V.D. Zwaag, Mater. Sci. Eng. R 143 (2021) 100590.
[20] Y.H. Mozumder, K.A. Babu, R. Saha, S. Mandal, Mater. Sci. Eng. A 823 (2021) 141725.
[21] N. Nejadsadeghi, A. Misra, Int. J. Mech. Sci. 185 (2020) 105867.
[22] Y.K. Dong, Z.G. Lin, L. Sun, Z.L. Xiong, Y. Luo, J. Wang, J. Plast, Eng. 25 (2018) 161–167.
[23] J. Park, M. Kang, S.S. Sohn, S.H. Kim, H.S. Kim, N.J. Kim, S. Lee, Mater. Sci. Eng. A 684 (2017) 54–63.
[24] M. Kang, J. Park, S.S. Sohn, H.S. Kim, N.J. Kim, S. Lee, Mater. Sci. Eng. A 693 (2017) 170–177.
[25] Q.F. Dai, R.B. Song, W.Y. Fan, Z.F. Guo, X.X. Guan, Acta Metall. Sin. 48 (2012) 1160–1165.
[26] E. Cadoni, N.K. Singh, D. Forni, M.K. Singha, N.K. Gupta, Eur. Phys. J. Spec. Top. 225 (2016) 409–421.
[27] X.C. Feng, X.Y. Liu, S.X. Bai, Y.C. Ye, L. Zong, Y. Tang, Mater. Sci. Eng. A 879 (2023) 145182.
[28] X.X. Dong, Y.F. Shen, W.Y. Xue, N. Jia, Mater. Sci. Eng. A 803 (2021) 140504.
[29] J.L. Dai, J. Yuan, Z.X. Yang, C.Q. Zhang, H. Zhang, S.Q. Yu, J. Mater. Res. Technol. 18 (2022) 3798–3807.
[30] S.Y. Lee, S. Chettri, R. Sarmah, C. Takushima, J. Hamada, N. Nakada, J. Mater. Sci. Technol. 133 (2023) 154–164.
[31] W.C. Hsu, T.E. Shen, Y.C. Liang, J.W. Yeh, C.W. Tsai, Acta Mater. 253 (2023) 118981.
[32] B. Sun, N. Vanderesse, F. Fazeli, C. Scott, J. Chen, P. Bocher, M. Jahazi, S. Yue, Scripta Mater. 133 (2017) 9–13.
[33] S.Y. Lee, C. Takushima, J. Hamada, N. Nakada, Acta Mater. 205 (2021) 116560.
[34] T.R. Jacobs, D.K. Matlock, K.O. Findley, Int. J. Plast. 123 (2019) 70–85.
[35] G. Tian, J. Xiao, Z.Y. Bao, S. Yao, L. Yan, A.M. Zhao, Mater. Sci. Eng. A 905 (2024) 145943.
[36] Y.Y. Cheng, G. Zhao, D.M. Xu, X.P. Mao, S.Q. Bao, G.W. Yang, J. Mater. Res. Technol. 20 (2022) 1226–1242.
[37] J.H. Nam, S.K. Oh, M. Park, Y.K. Lee, Acta Mater. 206 (2021) 116613.
[38] Z.H. Cai, H. Ding, R.D.K. Misra, H. Kong, Scripta Mater. 71 (2014) 5–8.
[39] J.H. Ryu, J.I. Kim, H.S. Kim, C.S. Oh, H. Bhadeshia, D.W. Suh, Scripta Mater. 68 (2013) 933–936.
[40] M. Azrin, G.B. Olson, R.A. Gagne, Mater. Sci. Eng. 23 (1976) 33–41.
[41] S.I. Baik, R.K. Gupta, K.S. Kumar, D.N. Seidman, Acta Mater. 205 (2021) 116568.
[42] P. Dadras, J.F. Thomas, Metall. Trans. A 12 (1981) 1867–1876.
[43] H. Liu, X.K. Shang, B.B. He, Z.Y. Liang, Int. J. Plast. 161 (2023) 103495.
[44] Y.Z. Li, Z.Y. Liang, M.X. Huang, Int. J. Plast. 150 (2022) 103198.
[45] T. Ungár, I. Dragomir, Á. Révész, A. Borbély, J. Appl. Crystallogr. 32 (1999) 992–1002.
[46] T. Ungár, A. Borbély, Appl. Phys. Lett. 69 (1996) 3173–3175.
[47] S. Sun, W. Zai, Y. Chen, L. Zhao, G.X. Sun, J.J. Hu, S. Han, J.S. Lian, Mater. Sci. Eng. A 839 (2022) 142802.
[48] B.E. Warren, Progr, Metal Phys. 8 (1959) 147–202.
[49] J. Chen, S. Lu, Z.Y. Hou, W.W. Song, Z.Y. Liu, G.D. Wang, T. Furuhara, Acta Mater. 271 (2024) 119832.
[50] J.Z. Zhang, Z.B. Dai, L.Y. Zeng, X.W. Zuo, J.F. Wan, Y.H. Rong, N.L. Chen, J. Lu, H. Chen, Acta Mater. 217 (2021) 117176.
[51] E. Tkachev, S. Borisov, Yu Borisova, T. Kniaziuk, A. Belyakov, R. Kaibyshev, Mater. Sci. Eng. A 895 (2024) 146212.

[52] T. Jiang, B.B. He, J.J. Sun, X.K. Shang, H. Yu, L.J. Xu, K.M. Pan, S.Z. Wei, Y.N. Liu, M.X. Huang, Mater. Charact. 214 (2024) 114059.
[53] M. Shimotomai, Metall. Mater. Trans. A 47 (2016) 1052–1060.
[54] Y. Ohmori, I. Tamura, Metall. Trans. A 23 (1992) 2737–2751.
[55] Y. Kawahara, K. Kaneko, H. Sawada, J. Takahashi, Acta Mater. 252 (2023) 118919.
[56] Y. Kawahara, T. Maeda, K. Kinoshita, J. Takahashi, H. Sawada, R. Teranishi, K. Kaneko, Mater. Charact. 183 (2022) 111579.
[57] Y. Imanami, M. Murakami, N. Nakada, T. Tsuchiyama, S. Takaki, ISIJ Int. 49 (2009) 1225–1228.
[58] S.L. Zhang, W. Zhou, S.B. Zhou, F. Hu, S. Yershov, K.M. Wu, J. Mater. Res. Technol. 24 (2023) 2385–2402.
[59] J.L. Dai, J. Yuan, Z.X. Yang, C.Q. Zhang, H. Zhang, S.Q. Yu, J. Mater. Res. Technol. 18 (2022) 3798–3807.